Journal of Applied Fluid Mechanics, Vol. 19, No. 1, pp. 3312-3323, 2026. Available online at www.jafmonline.net, ISSN 1735-3572, EISSN 1735-3645. https://doi.org/10.47176/jafm.19.1.3604



Electrohydrodynamic Flow and Particle Dynamics in Four-shaped Electrostatic Precipitators via a Modified Eulerian Approach

H. Shen ¹, W. Wang ¹, W. Yu ², Y. Zheng ¹, G. Hou ¹, and Y. Kang ^{3†}

¹ Department of Refrigeration and Air Conditioning, Shanghai Ocean University, Shanghai, 201306, China
² Department of Energy Conservation, China Testing & Certification International Group Shanghai Testing Limited Company, Shanghai, 201210, China

³ College of Environmental Science and Engineering, Donghua University, Shanghai, 201620, China

†Corresponding author. E-mail address: ymkang@dhu.edu.cn

ABSTRACT

Electrostatic precipitators (ESPs) are essential for particulate removal from industrial emissions, yet the investigation of the influence of electrode geometry and arrangement on the flow patterns, electrical characteristics, and collection efficiency remains insufficient. In the present study, the finite volume method in ANSYS Fluent with User-Defined Functions is employed to simulate the flow pattern and particle transportation in duct-type ESPs for four dischargecollecting configurations (i.e., combinations of rod-wire corona electrode with planar and wavy collecting plates). The results reveal that the corona electrode's geometry plays a key role in determining the electric field strength, charge distribution, and ionic wind generation in the channels, while the collecting plate's curvature primarily influences the field intensity near its surface. In the wavy plate channel, evident vortices appear in the concave area adjacent to the collecting wall at a moderate inlet velocity ($u_0 = 0.5 \text{ m/s}$), which enhances the local flow that favors particle deposition and thus improves collection efficiency. At a high inlet velocity ($u_0 = 1.0 \text{ m/s}$), the enhancement effect attributed to flow-induced deposition is reduced in all four channels because the flow acceleration caused by electric wind adversely affects the collection efficiency. The numerical results provide practical information for optimizing the design of the electrode structure and the channel configuration to improve the ESP performance under varying operational parameters.

Article History

Received April 20, 2025 Revised July 18, 2025 Accepted August 8, 2025 Available online November 5, 2025

Keywords:

Electrohydrodynamic flow Numerical simulation Collecting plate Discharge electrode Particle collection

1. Introduction

Air pollution in China and some other developing countries has attracted sustained attention in the past few decades, primarily because of the emission of particulate matter, especially fine particulate matter. This pollution has contributed to a decline in urban air quality and presents severe health risks to the residents (Iranshahi et al., 2024; Jin et al., 2016). To address this challenge, electrostatic precipitators (ESPs) have emerged as a leading solution for fine particle collection with high efficiency (Adamiak, 2013; Iranshahi et al., 2024; Parker, 2012).

A standard ESP channel consists of two grounded, parallel plates that act as collecting electrodes (i.e., collecting plates), with a row of wires arranged along the centerline between them serving as discharge electrodes (i.e., discharge wires). The design and arrangement of the

electrodes are critical for enhancing the charging and retention of particles within ESP channels. For example, discharge electrodes featuring spikes are recognized for generating elevated corona currents, thereby improving particle charging in ESPs (Brocilo et al., 2008; Fujishima et al., 2004; Podlinski et al., 2013). Furthermore, incorporating cavities into collecting plates has been demonstrated to alleviate the re-entrainment of particles deposited on these surfaces (Bernstein & Crowe, 1981; Brocilo et al., 2008; Deepthi et al., 2022).

Within the ESP channel, corona discharge generates a complex turbulent, particle-laden flow driven by the dynamic interaction between the primary flow (also called the mainflow or inlet flow) and the secondary flow (often known as electric wind or corona wind) (Ekin & Adamiak, 2023; He et al., 2023; Iranshahi et al., 2024). Over the past several decades, extensive investigations have been conducted on the performance of ESP channels featuring

N	NOMENCLATURE						
a_k	constants	N_i	ion concentration				
a_{ε}	constants	p	gas pressure				
b	half-height of the wavy plate	$q_{ m p}$	particle charge				
B_{e}	electrical mobility of the charged particle	r_0	rod discharge wire radius				
C	concentration of particle	r_{S}	tip radius of star-shaped wire				
C_0	inlet particle concentration	S_x	wire-to-wire spacing				
$C_{1arepsilon}$	constants	S_{y}	wire-to-plate spacing				
C_{c}	Cunningham correction factor	\dot{T}	gas temperature, $T = 298.15 \text{ K}$				
C_i	thermal velocity of the ions	t	particle residence time				
D_{B}	particle diffusion coefficients accounting for the Brownian motion	u_0	inlet velocity				
D_{e}	ion diffusivity (ranging from 0.01 to 0.1 m ² /s)	U_0	applied electric potential at the discharge electrode				
d_{p}	particle diameter	u_i	gas velocity component in the x_i -direction				
$D_{ m T}$	particle diffusion coefficients accounting for the turbulent flow	W	width and height of the star-shaped wire				
e	electronic unit charge, $e = 1.6 \times 10^{-19} \mathrm{C}$						
E	magnitude of local electric field strength	τ	constants of time ($\tau = 4\varepsilon_0/\rho_{\rm ion}k_{\rm ion}$)				
E(x)	electric field intensity along the <i>X</i> -direction	γ	determined by the ratio of electric current				
()	, .	,	from the preceding two iterations				
$E_{\rm ave}$	average electric field strength in the ESP channel	φ	electric potential				
$E_{\rm i}$	component of the electric field intensity in the x_i -direction	λ	mean free path of the gas molecules, $\lambda =$				
Г	•		0.065 μm at 25°C				
$E_{ m Pee}$ k	electric field intensity calculated by Peek's formula	${\cal E}$	turbulent dissipation rate, and the constants				
$E_{ m q}$	numerical solution	$ au_{ m c}$	constants of time $(\tau_c = 8\varepsilon_0 k_B T/d_p C_i N_i e^2)$				
$E_{ m w}$	electric field intensity on the discharge surface	ρ	gas mass density				
$G_{\rm k}$	generation of turbulence kinetic energy owing to the gas velocity gradients	$ ho_{ ext{w}}$	ion charge density predicted by Kaptzov's approximation				
Ι	specific current of the discharge wire	ρ ion	ion charge density on the discharge surface				
J(x)	space charge density along the X-direction	$ ho_{ m ion}E_{ m i}$	electrical body force, expressing the coupling interaction between electric field and fluid flow				
$J_{ m p}$	average current density at the plate	ε_0	permittivity of free space				
k	turbulent kinetic energy	\mathcal{E}_{p}	relative dielectric constant of the particle				
k_B	Boltzmann constant, $k_B = 1.38 \times 10^{-23} \text{ J/K}$	μ	gas dynamic viscosity				
$k_{\rm ion}$	positive ion mobility, $k_{\text{ion}} = 1.8 \times 10^{-4} \text{ m}^2/(\text{V} \cdot \text{s})$	μ eff	effective turbulent (or eddy) kinematic viscosity				
L	length of collecting plate	μ_t	turbulent dynamic viscosity				
n	number of iterations	β	under-relaxation factor				
11	namosi di namuni	ρ	under reluxurion nucloi				

increasingly complex geometric electrode configurations, with the aim of enhancing particle removal efficiency (Adamiak, 2013; Lee, 2024; Parker, 2012). However, most analytical solutions (Adamiak, 2013; Lei et al., 2008; Soldati, 2000) focus on simpler configurations of smooth wires or flat collecting plates, and the study on ESPs with collecting electrodes of special shapes is still limited so far (Bernstein & Crowe, 1981; Choi et al., 2021; Park & Kim, 2000; Shen et al., 2018) or discharge electrodes (Chen et al., 2021; Hao et al., 1990; Sander et al., 2018; Shen et al., 2020).

Numerous studies have concentrated on the performance of collecting electrodes. For example, Bernstein and Crowe (1981) conducted analytical investigations into the electrical characteristics and flow patterns within an ESP channel utilizing W-type plates (i.e., wavy plates or ZT-24 plates). Park and Kim (2000)

investigated the impacts of the electrohydrodynamic (EHD) flow on charged-particle behaviors in the ESP with the cavity plate using both experimental and numerical methods. More recently, Shen et al. (2018) further analyzed the flow regimes in the channels constructed with five collecting plates, and Zhou et al. (2021) carried out a comparable study to investigate the flow patterns and particle behaviors in ESP with various collecting shapes. In addition, the results by Choi et al. (2021) showed how parameters related to the wavy plate, including the wavelength and amplitude, influence the ESP performance. However, many of these studies simplified the geometric structure of the discharge electrode, which is typically assumed to be a perfectly smooth wire that produces homogeneous discharge.

In contrast, other studies have focused exclusively on the corona characteristics of discharge electrodes, often overlooking the collection electrodes. For instance, Hao et al. (1990) measured the electric field strength close to the collecting plate for three types of wires: star–shaped, sawtooth spike, and tube–type spike. Sander et al. (2018) compared the collection efficiencies of symmetric and asymmetric spiked wire–plate ESPs by both experimental measurements and the Deutsch equation. Shen et al. (2020) evaluated the vortex strength and turbulence intensity produced by secondary flow in ESPs with six–shaped wires (including round–type wires, knife–shaped wires, two star–shaped wires, and others), employing the FLUENT code. Chen et al. (2021) experimentally investigated the ionization characteristics of RS and BS wires in the channel with C-type plates.

Additionally, several other studies have examined specific electrode (spike electrode) configurations, though their investigations were limited exclusively to the spikewire geometry. Brocilo et al. (2008) studied the electrical characteristics in ESPs with three different collecting plates. The results by Fujishima et al. (2004) show that the flow near the wall of the concave part of the collecting plate is relatively slow and stable, which is beneficial for the deposition of the charged aerosols. In contrast, the convex zone has minimal impact on the primary flow. For the C-type ESP, the electrical field distribution and the EHD characteristics in the channel with spiked corona wires were also investigated by others (Neimarlija & Muzaferija, 2011; Farnoosh et al., 2011; Podlinski et al., 2013). For instance, the results by Podlinski et al. (2013) showed how the positioning of spike points relative to the flow direction changes the flow pattern within the channel.

Although the above-mentioned studies have made significant contributions to understanding the electrical characteristics, flow patterns, and particle dynamics of ESPs, few studies have considered the geometries of both the corona and collecting electrodes simultaneously. To bridge this gap, the present study explores four distinct discharge-collecting configurations, combining two shaped discharge electrodes and two types of collecting electrodes, to evaluate their combined impact on ESP performance. The simulations incorporate finite volume solvers for the electric field, charge density, and particle concentration within an Eulerian framework while considering electrostatic forces. The interaction among these solvers is facilitated by employing user-defined functions (UDFs). A comparison of these four configurations provides valuable insights into the complex relationship between electrode configuration and ESP performance.

2. GEOMETRICAL CONFIGURATION

Four discharge–collecting systems with defined computational domains are assumed to explore the ESP performance, as shown in Fig. 1. The electrodes used in the simulation cases are the combinations of two discharge wires (rod wire and star–shaped wire) and two collection plates (flat plate and wavy plate). Table 1 summarizes the abbreviations used for the four discharge–collecting configurations. The key dimensions and operational parameters of the four referenced systems are illustrated in Fig. 1 and listed in Table 2, respectively.

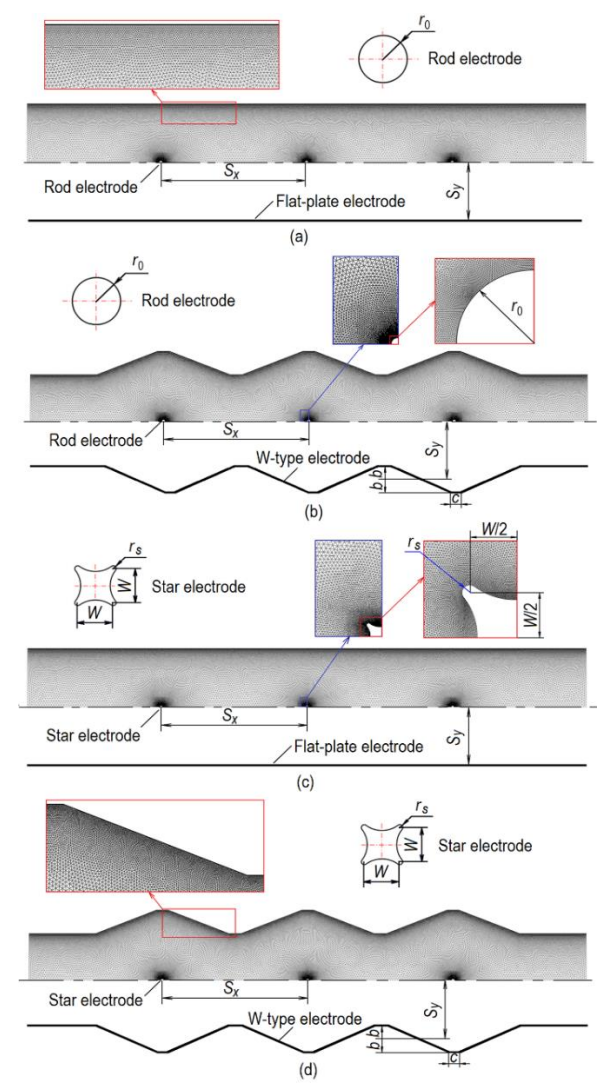


Fig. 1 Schematics of the ESP channel and computational domain with four discharge-collecting systems: a) R-F system, b) R-W system, c) S-F system, and d) S-W system (Table 1)

Table 1 Four discharge-collecting systems in the electrostatic precipitator channels

Discharge	Collecting plate		
wire	flat-type (F)	W-type (W)	
rod-type (R)	R-F system	R-W system	
star-type (S)	S–F system	S-W system	

Furthermore, the GCI (Grid Convergence Index) criterion, as established by Roache (1994), was successfully met for all configurations of this study, ensuring the robustness of the numerical results. Previous studies (Shen et al., 2018; 2020) provide detailed explanations of the grid independence tests. The computational domains were discretized via nonuniform grids of 170,400, 172,970, 180,984, and 184,614 cells for the respective channels.

3. COMPUTATIONAL MODEL AND PROCEDURE

3.1 Governing Equations

The flow within an ESP is modeled as an isothermal, incompressible, and steady turbulent flow. Incorporating

Table 2 Values of the main parameters of the four discharge-collecting systems

<i>S_x</i> (m)	<i>S_y</i> (m)	<i>b</i> (m)	c (m)	r ₀ (mm)	r _S (mm)	W (mm)	$D_{ m e} \ ({ m m}^2 \ { m s}^{-1})$	<i>U</i> ₀ (kV)
0.24	0.15	0.02	0.02	1.25	0.25	4	0.1	70

external body forces such as the Coulomb force, the governing equations for describing the flow in the channel are as follows (He et al., 2023; Iranshahi et al., 2024; Kodi et al., 2023):

$$\frac{\partial}{\partial x} \left(\rho u_j \right) = 0 \tag{1}$$

$$\frac{\partial}{\partial x_{i}}(\rho u_{i}u_{j} - (\mu + \mu_{t})\frac{\partial u_{i}}{\partial x_{i}}) = -\frac{\partial p}{\partial x_{i}} + \rho_{\text{ion}}E_{i}$$
 (2)

where ρ and ρ_{ion} are the mass density and ion charge density of the gas, respectively. u_i and u_j are the velocity components in the i- and j-direction (i, j = x, y, z), respectively, and p represents the gas pressure. The coefficients μ and μ_t are the viscosity of dynamic and turbulent, respectively. $\rho_{\text{ion}}E_i$ is the electrical body force in the i-direction, representing the coupling between the flow and the electrical field.

The Coulomb force in Eq. (2), i.e., $\rho_{\text{ton}}E_i$, is determined by using the finite volume solver from the numerical solution of the electric characteristic equations, i.e.,

Poisson's equation

$$\nabla^2 \varphi = -\rho_{\text{ion}} / \varepsilon_0 \tag{3}$$

and current continuity equation

$$\frac{\partial}{\partial x_{j}} \left(\rho \rho_{\text{ion}} \left(k_{\text{ion}} E_{j} + u_{j} \right) \right) = \rho D_{e} \frac{\partial^{2} \rho_{\text{ion}}}{\partial x_{j}^{2}}$$
(4)

where $E_j = \partial \varphi / \partial x_j$, with φ the electrical potential. The positive ion mobility is set as $k_{\text{ion}} = 1.8 \times 10^{-4} \text{ m}^2/(\text{V} \cdot \text{s})$ (Oglesby & Nichols, 1978; Parker, 2012). The value of the ion diffusivity D_e ranges from 0.01 to 0.1 m²/s (Bentz, 2000; Skodras et al., 2006).

To balance the computational cost and accuracy, we adopt the RNG (Renormalization Group) k- ε model—extensively used in prior studies (Choi et al., 2021; & Kim., 2000; Shen et al., 2020)—to simulate the flow regimes in the ESP. The equations to calculate the kinetic energy k and dissipation rate ε are written as (Park & Kim, 2000; Neimarlija & Muzaferija, 2011):

$$\frac{\partial}{\partial x_{i}}(\rho k u_{j} - a_{k} \mu_{\text{eff}} \frac{\partial k}{\partial x_{i}}) = G_{k} + \rho k \tag{5}$$

$$\frac{\partial}{\partial x_{i}} (\rho \varepsilon u_{j} - a_{\varepsilon} \mu_{\text{eff}} \frac{\partial \varepsilon}{\partial x_{i}}) = C_{1\varepsilon} G_{k} \frac{\varepsilon}{k} + C_{2\varepsilon} \rho \frac{\varepsilon^{2}}{k}$$
 (6)

where μ_{eff} is the effective turbulent viscosity, and the term G_k of Eq. (5) is the generation of k due to the velocity gradients. The values of the constants contained in the above equations are $a_k = a_{\varepsilon} = 1.39$, and $C_{1\varepsilon}$ and $C_{2\varepsilon}$ take the values of 1.42 and 2.0, respectively.

The Eulerian approach is used to describe particle dynamics in the channels, treating particles as secondary fluids and formulating equations for their average properties (Behroyan et al., 2015; Chu et al., 2023; Ganesan et al., 2016; Sivasankaran & Mallawi, 2021). When electric forces are exerted on the charged particles, the modified convective-diffusion equation governing the distribution of particle concentration *C* is (Chu et al., 2023; Kodi et al., 2023; Park & Kim, 2000; Schmid & Vogel, 2003):

$$\frac{\partial}{\partial x_{j}} \left(\left(u_{j} + B_{e} E_{j} \right) C \right) = \frac{\partial C}{\partial x_{j}} \left(\left(D_{B} + D_{T} \right) \frac{\partial C}{\partial x_{j}} \right) \tag{7a}$$

where $D_{\rm B}$ and $D_{\rm T}$ are particle diffusivities due to the Brownian and turbulent diffusions, respectively. $q_{\rm p}$ denotes the charge on the particle with a diameter $d_{\rm p}$. The Cunningham slip correcting factor, $C_{\rm c}$, calculated by (Friedlander, 2000):

$$C_c = 1 + (1.257 + 0.4\exp(-1.1d_p/2\lambda))2\lambda/d_p$$
 (7b)

where λ is the mean free path of air molecules, with the value is approximately 0.065 μ m at 25°C.

The predominant particle charging mechanisms in ESPs are field charging and diffusion charging. This study focuses on fine particles with $d_{\rm p}=0.5~\mu{\rm m}$, which are difficult to remove via traditional dust removal mechanisms. For particles with $d_{\rm p}<1~\mu{\rm m}$, both charging mechanisms occur simultaneously. These particles are assumed to be neutral before they enter the ESP channel. The total charge of a single particle $q_{\rm p}$ is calculated by (Friedlander, 2000):

$$q_{\rm p} = \pi \frac{3\varepsilon_0 \varepsilon_{\rm p}}{\varepsilon_{\rm p} + 2} E d_{\rm p}^2 \frac{t}{t + \tau} + \frac{2\pi\varepsilon_0 d_{\rm p} k_{\rm B} T}{e} \ln(1 + \frac{t}{\tau_{\rm c}})$$
(8)

with

$$\tau = 4\varepsilon_0/\rho_{\rm ion}k_{\rm ion} \tag{8a}$$

$$\tau_{\rm c} = 8\varepsilon_0 k_{\rm B} T / d_{\rm p} C_{\rm i} N_{\rm i} e \tag{8b}$$

where $\varepsilon_{\rm p}$ and t represent the relative permittivity and the residence time of the charged particles, respectively. The Boltzmann constant, $k_{\rm B}$, is equal to 1.38×10^{-23} J/K, and the gas temperature, T, is set to 298.15 K. The elementary charge is represented by e, with a value of 1.6×10^{-19} C. The thermal velocity of the ions C_i takes the value of 2.4×10^{22} m/s. Additionally, the ion concentration can be expressed as $N_i = J_{\rm p}/k_{\rm ion}E$, with $J_{\rm p}$ is the current density at the collecting plate.

3.2 Boundary Conditions and Computational Procedure

Table 3 provides an overview of the boundary conditions for the four proposed ESP configurations.

The initial value of the space charge density adjacent to the discharge electrode, ρ_w , is predicted *via* Kaptzov's approximation (Lei et al., 2008). When performing the iterative calculation, the *n*th round ρ_w is updated using the following equation:

Table 3 Boundary conditions for simulating the ES	Table 3 Boundar	v conditions for	simulating th	ie ESP
---	-----------------	------------------	---------------	--------

	Surfaces				
Field	Inlet	Outlet	Corona	Collecting	
		Outlet	electrode	electrode	
Airflow	Velocity-	Pressure-	Wall	Wall	
Allilow	inlet	out	wan	vvall	
Electric	2 42/24-0	$\partial \varphi / \partial n = 0$	70 kV	0 kV	
potential	$\partial \varphi / \partial n = 0$	$O\varphi/On=0$	/ U K V	UKV	
Space charge	a /a /a /a	a /a /a /a	Peek	3 ~ /3 ~ _ 0	
density	$\partial \rho_{\text{ion}}/\partial n=0$	$\partial \rho_{\text{ion}}/\partial n=0$	formula	$\partial \rho_{\text{ion}}/\partial n=0$	
Particle	$C=C_0$	$\partial C/\partial n=0$	C=0	∂ <i>C</i> /∂ <i>n</i> =0	
concentration	C-C0	CC/CH=0	C-0	0C/0H=0	

$$\rho_{\rm w}^{n} = (1 - \beta) \rho_{\rm w}^{n-1} + \beta \rho_{\rm W}^{n-1} \left(E_{\rm w}^{n-1} / E_{\rm Peek} \right)^{\gamma}$$
 (9)

where n represents the iteration round, β denotes the under-relaxation factor, $E_{\rm w}$ is the field strength close to the surface of the discharge electrode, $E_{\rm Peek}$ is the calculated electric field by Peek's formula (Oglesby & Nichols, 1978; Parker, 2012), and γ is the ratio of the currents of the previous two iterations. The flowchart for the solution is depicted in Fig. 2, and the details on the implementation steps can be found in the supplementary.

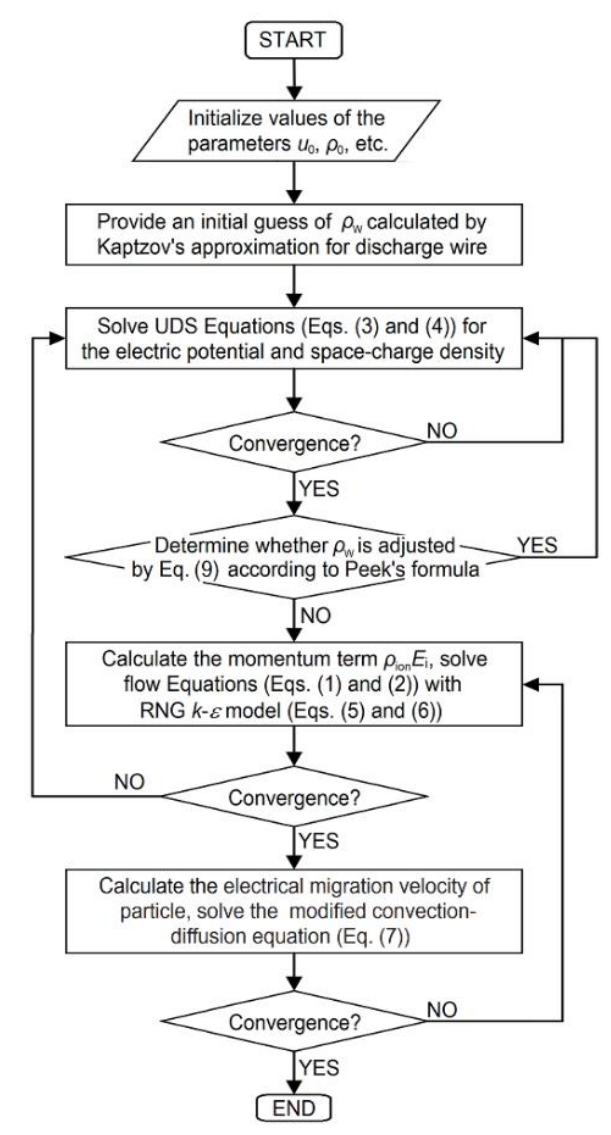


Fig. 2 Flowchart of the simulation

3.3 Model Validation

The reliability and accuracy of the model proposed in this study for predicting electric field strength were validated by using the test data of Penney and Matick (1960). As shown in Fig. 3, the calculated potential curves match very well with the measured data by Penney and Matick (1960), meaning that this model can accurately predict the electric field in the ESP channels.

The numerical results of the flow regime and particle transport in the ESP were also validated by comparing the simulations with the test results from Leonard et al. (1983) and Kihm (1987), respectively. The results are shown in Fig. 4.

Figure 4 shows a favorable agreement of velocity distributions between the gas velocity distributions derived from the simulations and those of the measurements by Leonard et al. (1983). Moreover, it is worth noting that both the experimental and simulation results indicate that the augmentation of the gas velocity (i.e., the flow acceleration effect), attributed to the electric wind within the center of the channel, becomes increasingly significant as the corona current intensifies (Yamamoto, 1981).

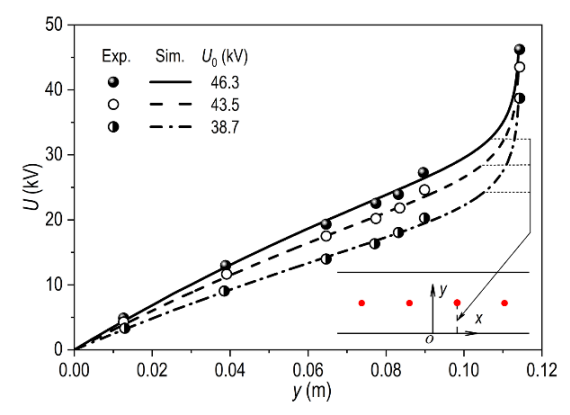


Fig. 3 Comparison of the electrical potential distributions in a wire-plate ESP channel between the numerical results and the experimental data (Penney & Matick, 1960) ($r_0 = 1 \text{ mm}$, $S_y = 114.3 \text{ mm}$, $S_x = 152.4 \text{ mm}$)

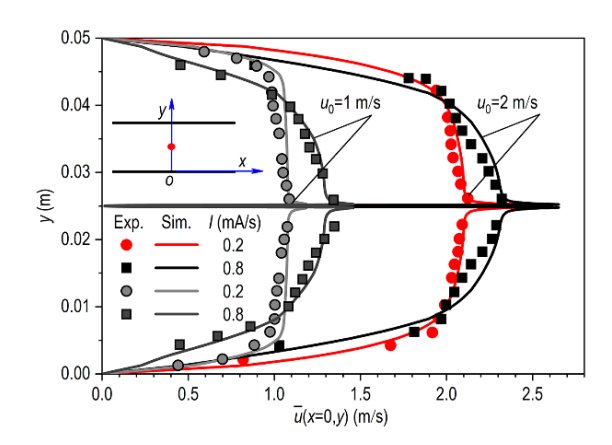


Fig. 4 Comparison of the mean velocity profile in the ESP channel between the numerical results and the test data by Leonard et al. (1983) ($r_0 = 0.1 \text{ mm}$, $S_y = 25 \text{ mm}$)

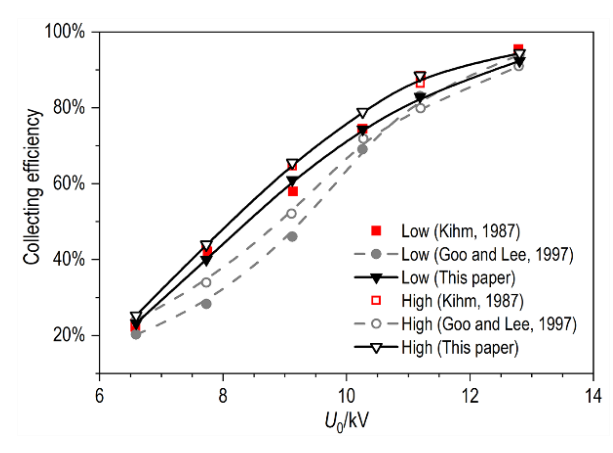


Fig. 5 Comparison of the collection efficiency between the results of this study and the experimental data (Kihm, 1987) and the simulations by Goo and Lee (1997) ($r_0 = 1 \text{ mm}$, $S_x = 50.8 \text{ mm}$, $S_y = 50 \text{ mm}$, $d_p = 4 \text{ \mu m}$, 'Low' and 'High' are the data for turbulent intensities at 1% and 30%, respectively)

The ESP verification model in this study, see Fig. 4(b), consists of a pair of flat plates and eight wires, which is consistent with the geometric structure of the experimental setup employed by Kihm (1987). As depicted in Fig. 5, the numerical results of this study show a more alignment with the test data by Kihm (1987) than the results by Goo and Lee (1997) across the applied voltage range.

4. RESULTS AND DISCUSSION

4.1 Electrical Characteristics

The electrical characteristics are simulated for four configurations *via* the present model. The results are shown in Figs. 6 to 9, where the dimensionless distances X and Y along the x- (i.e., flow direction) y- directions are defined as $X = 2x/S_x$, and $Y = y/S_y$, respectively.

Figures 6(a) to 6(d) present the numerical results of the electric field distributions within the ESP channels. It is easy to observe that the collecting plate's geometry significantly influences the distribution of electric field strength close to its surface, whereas the discharge electrode's structure primarily affects the magnitude of the intensity. Specifically, the rod wire generates a higher electric field intensity than the star–shaped wire, regardless of the collecting plate's structure. Moreover, in the flat–type channels, the electric field intensity in the vicinity of the surface facing the discharge electrode (X = 0 in Fig. 6(e)) is greater than that observed with the W–type plate.

Figures 7(a) to 7(d) show that the spatial distributions of charge density within the ESP channels are predominantly influenced by the discharge electrode's structure rather than the collecting electrode's shape. This suggests that ESP channels equipped with the same discharge electrode display similar space charge density profiles. Notably, a rod discharge wire produces a one-point corona, as shown in Figs. 7(a) and 7(b), whereas a star—shaped discharge wire creates four corona points, as depicted in Figs. 7(c) and 7(d). Compared with the rod wire, the corona shielding effect of the star—shaped wire

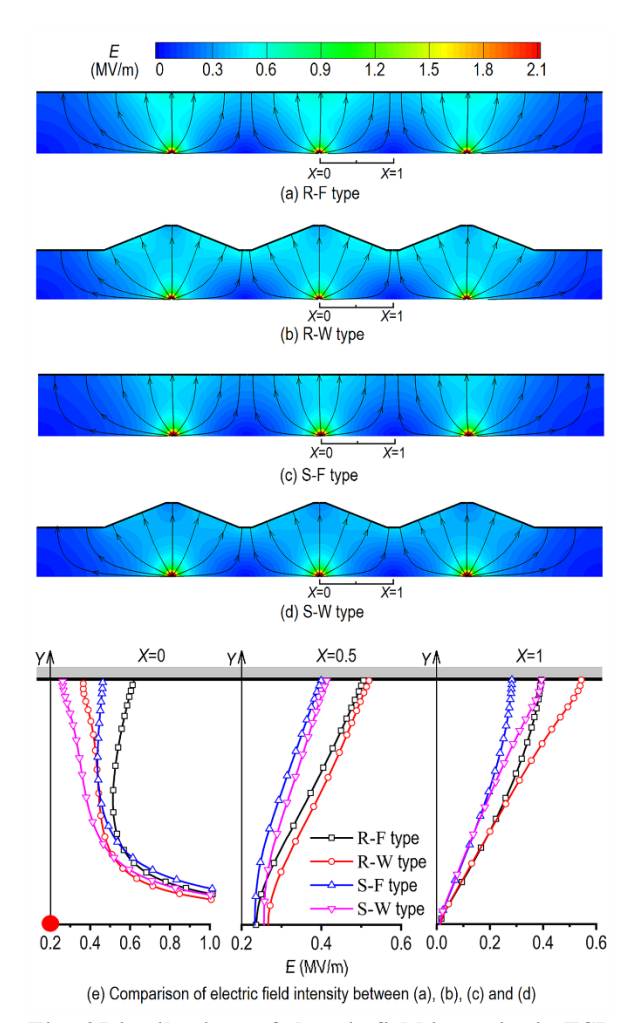


Fig. 6 Distributions of electric field intensity in ESP channels with four discharge—collecting configurations

results in a weaker corona field. Consequently, the ESP channel featuring the star–shaped wire, depicted in Fig. 7(e), has a lower space charge density.

The electrical characteristics near the collection surface are crucial for particle capture and the stable operation of ESPs in practical applications (Bernstein & Crowe, 1981; Hao et al., 1990). Figure 8 illustrates the variations of E(X) and J(X) along the X direction, close to the collecting surface, for the four configurations. Meanwhile, Table S2 provides a clear overview of how these configurations affect the distribution of the electric field and its uniformity across the electrode surface.

The results in Fig. 8 show that the collecting plate's shape significantly influences the distributions of E and J near the collector surface, while the magnitudes of these two electrical parameters are primarily impacted by the discharge wire's structure. On average, the values of E and J in the channels with star–shaped discharge wires are lower than those of rod wires. This deviation results from the corona shielding effect between adjacent corona locations on the star–shaped wire. In the flat–type channel, both E and E decrease along the E direction. In contrast, in the W–type channel, the distribution of electric field strength remains uniform within the range of 20% to 80% of the collection area. Additionally, the peak and valley values coincide with the bends of the collecting plate.

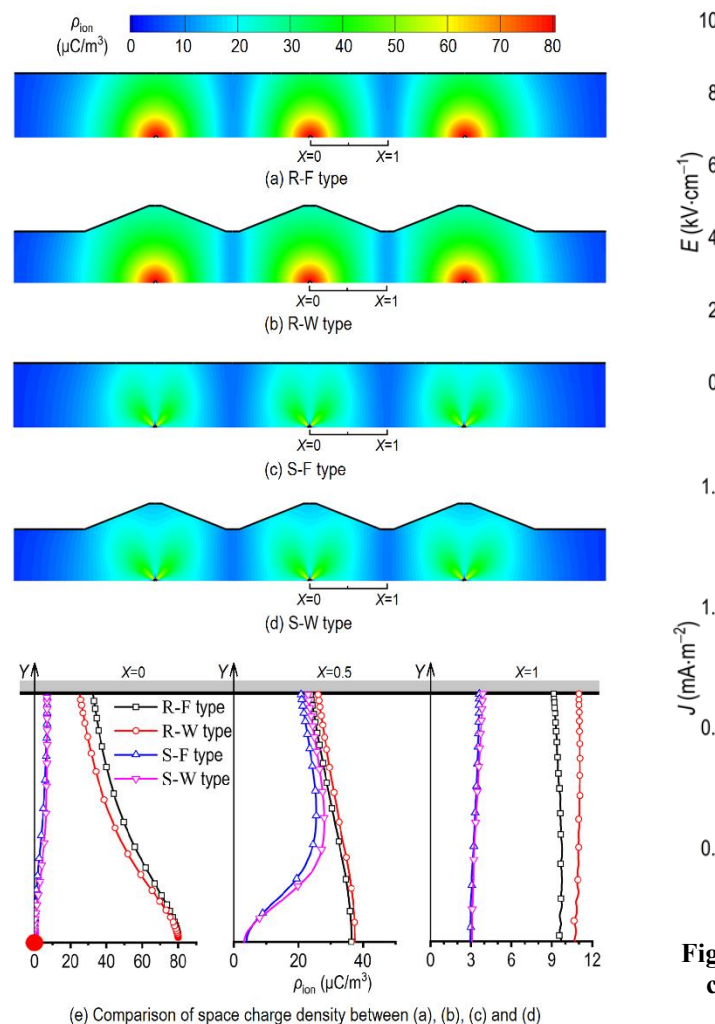


Fig. 7 Space charge density distributions in ESP channels with four discharge-collecting configurations

4.2 Electric Wind

The EHD flow has a dual impact, which affects the motion and capture of the charged particles on one hand, and also causes particles to escape from the collection surface, specifically the backmixing or resuspension of fine particles within an ESP channel (Farnoosh et al., 2011). Yamamoto and Velkoff (1981) emphasized the significant role played by the EHD flow in particle collection processes within an ESP channel with a R-F system, especially for submicron particles, due to the low migration velocity. Nikas et al. (2005) claimed that the presence of EHD flow within a R-F type channel, particularly at $u_0 = 1.0$ m/s, primarily diminishes the collection efficiency for small particles ($d_p = 4 \mu m$) rather than larger ones. Talaie (2005) found that reducing the inlet velocity exacerbates the negative effect of secondary flow on the particle removal efficiency for 3 µm particles in a R-F type channel.

Therefore, simulating the EHD flow pattern is conducted with three inlet velocities (i.e., $u_0 = 0$ m/s, 0.5 m/s, and 1.0 m/s) for the four discharge–collecting configurations. Figures 9 to 11 depict the gas velocity distributions and gas velocity vectors in the four systems, respectively.

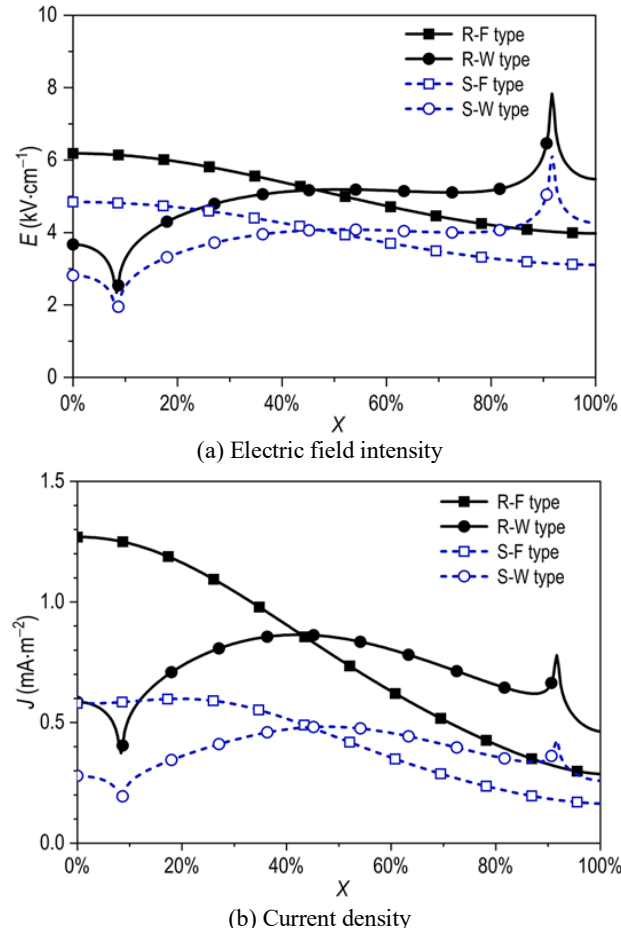


Fig. 8 Distribution of electrical characteristics on the collection surface in the four ESP configurations

Figures 9(a) to 9(d) vividly depict the occurrence of a sequence of vortices generated by the electric wind within the four ESP channels when there is no primary flow (i.e., $u_0 = 0$ m/s). These observations are highly consistent with the conclusions drawn from the previous studies (Yamamoto & Velkoff, 1981; Kallio & Stock, 1992). The strength of these vortices is greater within the ESP channel equipped with a flat-type collecting plate than within the W-type channel with an identical discharge electrode. Furthermore, when the collecting electrode has the same structure, the gas velocity close to the surface of the rod discharge wire is greater than that of the star-type wire (X)= 0.5 in Fig. 9(e)). Among the four discharge-collecting systems, the R-F configuration results in the most robust vortex strength (see Figs. 9(a) and 9(e)), followed by the channel with R-W (Fig. 9(b)) and the S-F systems (Fig. 9(c)), while the S–W system (Fig. 9(d)) shows the weakest vortex and the smallest region influenced by the secondary

It is found in Fig. 10 that the vortices in the S–F system near the collecting plate nearly disappear as u_0 increases to 0.5 m/s, see Fig. 10(c). In contrast, the corona wind-induced vortices in the other channels are advected toward the collection plates by the primary flow. Among these scenarios, the R–W system shows the most robust vortices, with the vortices covering the largest area (see Figs. 10(b) and 9(e)), followed by the S–W system (Fig. 10(d)) and the R–F system (Fig. 10(a)).

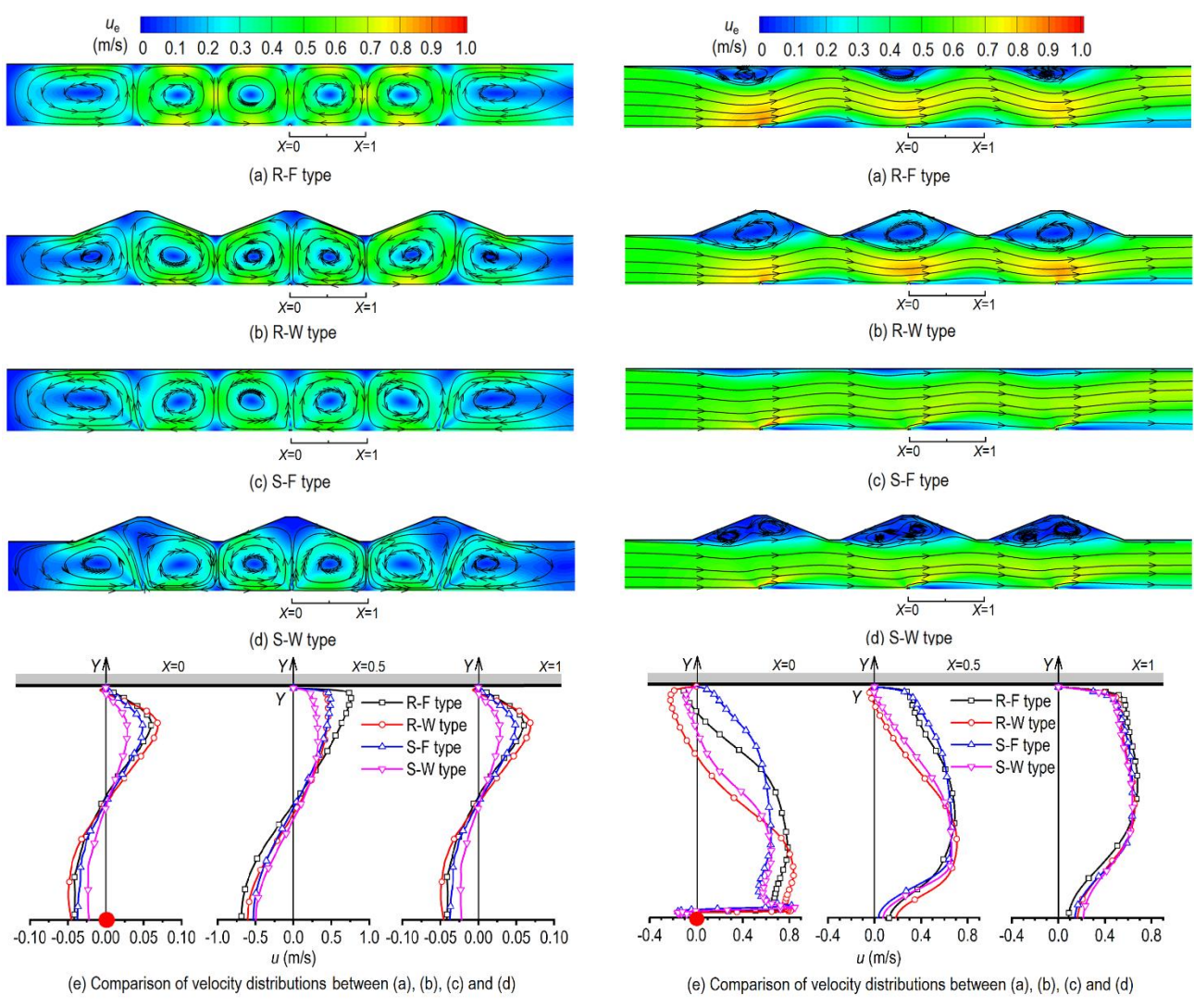


Fig. 9 Comparisons of the ionically induced flows among the four discharge–collecting systems ($u_0 = 0$ m/s)

Fig. 10 Comparison of the coupling flows among the four discharge–collecting systems ($u_0 = 0.5 \text{ m/s}$)

For the high inlet velocity, the numerical results presented in Figs. 11(a), 11(c), and 11(e) reveal that elevating u_0 to 1.0 m/s results in the dissipation of vortices caused by the electric wind in the mainflow region of the flat—type channels.

However, see Figs. 11(b), 11(d), and 11(e), regardless of whether electric wind is considered, the subtle vortices established by the geometric profile of the collecting plate continue to persist within the cavities of the W-type channel, thereby forming regions conducive to particle deposition, as discussed in previous studies (Fujishima et al., 2004; Dong et al., 2018; Wang et al., 2019). The only apparent effect of the secondary flow on the primary flow is to increase the local gas velocity (i.e., the flow acceleration effect), which is present across all four channels as u_0 increases to 1.0 m/s. It is worth noting that the acceleration effect within the flat-type channels is stronger than that inside the W-type channels (i.e., R-W (Fig. 11(b)) and S-W (Fig. 11(d)) systems). The most pronounced acceleration effect occurs in the R-F type channel (Fig. 11(a)), whereas the weakest acceleration effect is observed in the S-W system.

Furthermore, the re-entrainment of particles previously deposited on the collecting plate in an operating ESP can stem from various factors (Soldati, 2000), and one of these factors is the direct flushing impact of the flow on the collecting surface. When both the W-type and flat-type channels employ the identical discharge electrode, the gas velocity close to the surface of the W-type palte remains lower than that observed in the flat-type channel (i.e., R-F and S-F systems). Particularly, the airflow velocity approaching the surface of the W-type plate merely reaches 15% of the mainstream velocity. The surface of the flat plate is subjected to direct scouring by the airflow, in contrast to the W-type channel, as shown in Fig. 10 and Fig. 11. Therefore, the numerical results shown in Fig. 10(a) and Fig. 11(a) mean that for the four discharge electrode systems, the most extensive region is subjected to airflow scouring. The most pronounced acceleration of the primary flow occurs in the R-F type channels, and this may result in severe particle re-entrainment in an operating ESP (Bernstein & Crowe, 1981; Islamov, 2018).

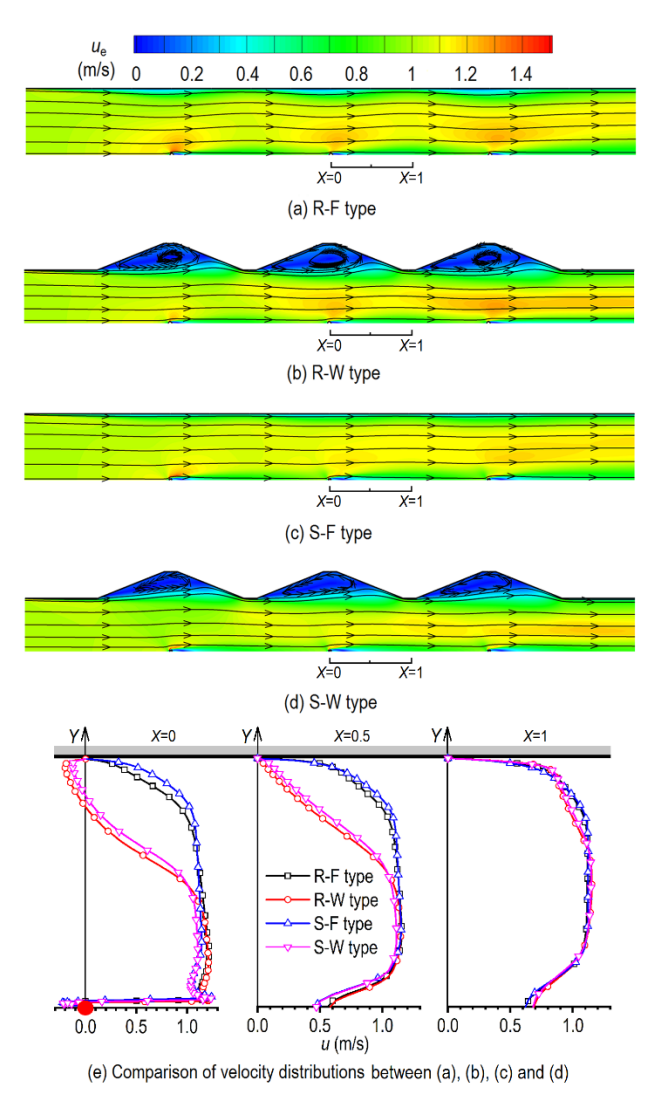


Fig. 11 Comparison of the coupling flows among the four discharge-collecting systems ($u_0 = 1.0 \text{ m/s}$)

4.3 Particle Transport and Collection

The simulations of particle transport are performed for the particles with a diameter of $d_{\rm p}=0.5~\mu{\rm m}$ and an inlet concentration of $C_0=1~{\rm mg/m^3}$, following the numerical solution of Eq. (7). The variations of the concentration in the four channels for $u_0=0.5~{\rm m/s}$ and $1.0~{\rm m/s}$ are presented in Fig. 12 and Fig. 13, respectively, where L is the length of the collection plate.

Figures 12(a) to 12(d) show that for the moderate inlet velocity, the impact of the vortices adjacent to the collection surface on the particle concentration is significant in all four discharge—collecting systems, and the stronger the vortex, the greater its effects. Evidently, this effect is more pronounced in the W-type channel than in the flat—type channel. As shown in Figs. 10(a) to 10(d) and Figs. 12(a) to 12(d), when passing through the discharge electrode, the flow splits mainly into two parts due to the impact of the vortices, one pushes the charged particles toward the collecting plate, while the other drives the particles away from the collecting surface and flows downstream. The results of Figs. 12(b) and 12(d) reveal that the former prevails over the latter in the W-type channel, leading to a higher particle removal efficiency

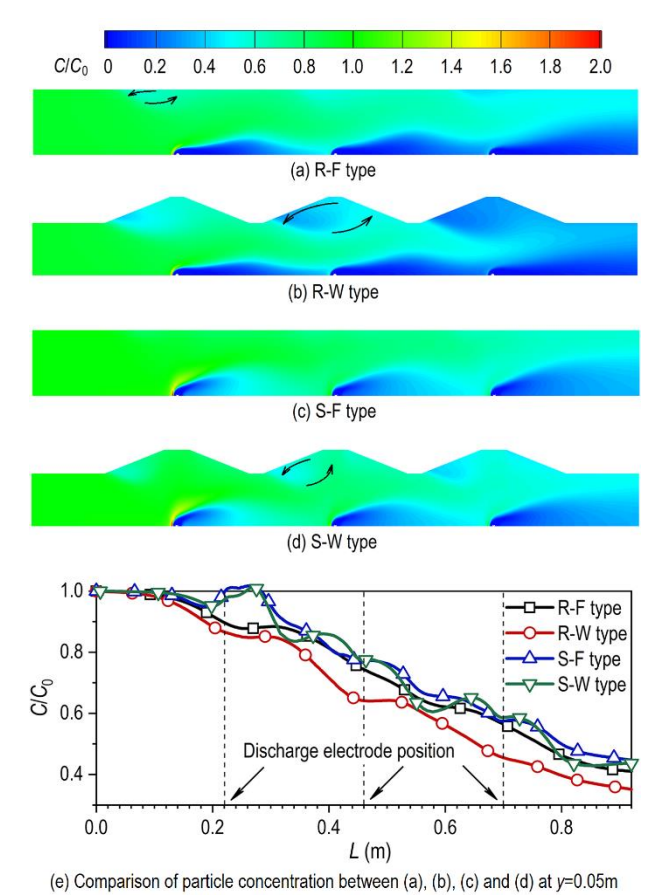


Fig. 12 Particle concentration distributions in the four discharge–collecting systems ($u_0 = 0.5 \text{ m/s}$)

than that in the flat-type channel with the same discharge electrode, as shown in Fig. 12(e).

As shown in Fig. 13, the impact of the vortex adjacent to the collecting surface on particle transportation is significantly reduced in all four discharge–collecting systems. Specifically, Fig. 13(b) shows that the vortex effect on the particle concentration is the most significant within the R–W system among the four systems, which has the strongest vortex strength (Fig. 11(e)). Furthermore, Fig. 13(e) indicates that the collection efficiency of the R–W system is higher than that of the R–F system. This difference is attributed to the more pronounced flow acceleration effect in the R–F system (Fig. 11(a)), where the acceleration induced by electric wind leads to an efficiency reduction.

The comparison between the S–F and the S–W system clearly shows that, as the inlet velocity increases, the influence of the vortex and the flow from the cavity region of the W–type plate on particle transport weakens, leading to only a slight difference in the collection efficiency between these two systems.

Both Figs. 12(e) and 13(e) show that due to the complex interaction between the electric wind and the charged particles, the concentration generally decreases in a fluctuating manner along the flow direction in all four discharge—collecting systems. The efficiency of the ESP channel with the rod-shaped wires is higher than that with the star-shaped wires because the former generates a stronger electric field intensity (Fig. 6(e)).

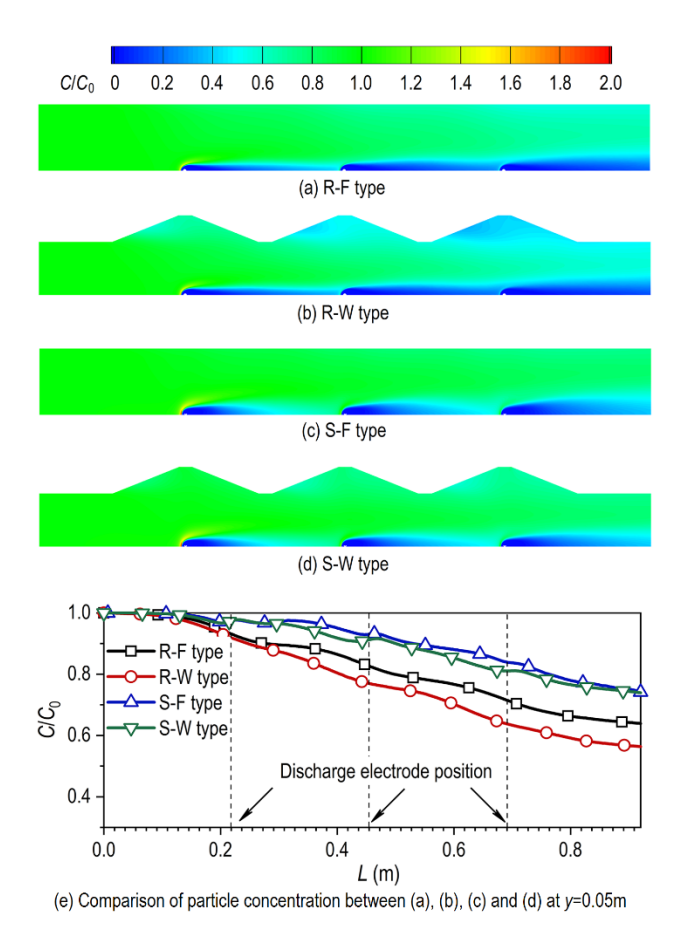


Fig. 13 Particle concentration distributions in the four discharge-collecting systems ($u_0 = 1.0 \text{ m/s}$).

5. SUMMARY AND CONCLUSIONS

An integrated mathematical model, based on the Eulerian approach and validated with experimental data, is proposed to simulate the electrical characteristics, EHD flow, and particle transport in the wire-duct ESP channel with four typical discharge—collection configurations. The main conclusions are as follows:

The corona position, mainly determined by the discharge electrode's structure, plays a significant role in the electrical characteristics of an ESP channel. On the contrary, the shape of the collecting plate has a more pronounced impact on the electric field strength close to the collecting wall than that of the discharge electrode. ESP channels with flat-type plates produce severe particle re-entrainment during the operation. Among the four discharge-collecting systems, the R–F system presents the highest level of re-entrainment, followed by the R–W and S–F systems, with the S–W system showing the lowest level of re-entrainment.

At a moderate inlet velocity ($u_0 = 0.5$ m/s), the secondary flow significantly influences both the flow and particle transport within the ESP channel. Between the F-type and W-type channels, the secondary flow in the latter is more effective at driving particles toward the collecting plates, thereby enhancing collection efficiency. At a high inlet velocity ($u_0 = 1.0$ m/s), the acceleration effect adversely affects the collection efficiency in all four channel configurations.

ACKNOWLEDGMENTS

This research was funded by the National Natural Science Foundation of China (Grant No. 42075179) and the Shanghai Ocean University Startup Fund for Young Scholars (Grant No. A2-2006-22-200312). The authors express their gratitude to Dr. D. Gottfried for his insightful comments and suggestions.

CONFLICT OF INTEREST

All the authors disclosed no relevant relationships.

AUTHORS CONTRIBUTION

Hen Shen: Investigation, conceptualization, project administration, resources, visualization, writing - review & editing, funding acquisition, supervision. Weihao Wang: Methodology, Data curation, Writing - review & editing. Wanxuan Yu: Formal analysis, writing - review & editing, supervision; Yonghao Zheng and Guanzhong Hou: visualization, writing - review & editing. Yanming Kang: Formal analysis, Writing - review & editing, Supervision. All the authors read and approved the final manuscript.

REFERENCES

.014

Adamiak, K. (2013). Numerical models in simulating wire-plate electrostatic precipitators: A review. *Journal of Electrostatics*, 71(4), 673-680. https://doi.org/10.1016/j.elstat.2013.03.001

Behroyan, I., Ganesan, P., He, S., & Sivasankaran, S. (2015). Turbulent forced convection of Cu–water nanofluid: CFD model comparison. *International Communications in Heat and Mass Transfer*, 67, 163-172. https://doi.org/10.1016/j.icheatmasstransfer.2015.07

Bentz, D. P. (2000). Influence of silica fume on diffusivity in cement-based materials: II. Multi-scale modeling of concrete diffusivity. *Cement and Concrete Research*, 30(7), 1121-1129. https://doi.org/10.1016/S0008-8846(00)00263-5

Bernstein, S., & Crowe, C. T. (1981). Interaction between electrostatics and fluid dynamics in electrostatic precipitators. *Environment International*, *6*(1), 181-189. https://doi.org/10.1016/0160-4120(81)90024-6

Brocilo, D., Podlinski, J., Chang, J. S., Mizeraczyk, J., & Findlay, R. D. (2008). Electrode geometry effects on the collection efficiency of submicron and ultra-fine dust particles in spike-plate electrostatic precipitators. *Journal of Physics: Conference Series*, 142(1), 012032. https://doi.org/10.1088/1742-6596/142/1/012032

Chen, B., Guo, Y., Li, H., Zhou, W., & Liu, B. (2021). Discharge characteristic of barbed electrodes in electrostatic precipitator. *Journal of Electrostatics*, 109, 103528. https://doi.org/10.1016/j.elstat.2020.103528

- Chu, Y.-M., Abbasi, A., Al-Khaled, K., Farooq, W., Khan, S. U., Khan, M. I., Eldin, S. M., & Guedri, K. (2023). Mathematical modeling and computational outcomes for the thermal oblique stagnation point investigation for non-uniform heat source and nonlinear chemical reactive flow of Maxwell nanofluid. *Case Studies in Thermal Engineering, 41*, 102626. https://doi.org/10.1016/j.csite.2022.102626
- Choi, H. Y., Park, Y. G., & Ha, M. Y. (2021). Numerical simulation of the wavy collecting plate effects on the performance of an electrostatic precipitator. *Powder Technology*, 382, 232-243. https://doi.org/10.1016/j.powtec.2020.12.070
- Deepthi, V. V. L., Lashin, M. M. A., Ravi Kumar, N., Raghunath, K., Ali, F., Oreijah, M., Guedri, K., Tag-ElDin, E. S. M., Khan, M. I., & Galal, A. M. (2022). Recent Development of Heat and Mass Transport in the Presence of Hall, Ion Slip and Thermo Diffusion in Radiative Second Grade Material: Application of Micromachines. *Micromachines*, 13(10), 1566. https://www.mdpi.com/2072-666X/13/10/1566
- Kodi, R., Ravuri, M. R., Veeranna, V., Ijaz Khan, M., Abdullaev, S., & Tamam, N. (2023). Hall current and thermal radiation effects of 3D rotating hybrid nanofluid reactive flow via stretched plate with internal heat absorption. *Results in Physics*, *53*, 106915. https://doi.org/10.1016/j.rinp.2023.106915
- Dong, M., Zhou, F., Zhang, Y., Shang, Y., & Li, S. (2018). Numerical study on fine-particle charging and transport behaviour in electrostatic precipitators. *Powder Technology*, 330, 210-218. https://doi.org/10.1016/j.powtec.2018.02.038
- Ekin, O., & Adamiak, K. (2023). Electric field and EHD flow in longitudinal wire-to-plate DC and DBD electrostatic precipitators: A numerical study. *Journal of Electrostatics*, 124, 103826. https://doi.org/10.1016/j.elstat.2023.103826
- Farnoosh, N., Adamiak, K., & Castle, G. S. P. (2011). Three-dimensional analysis of electrohydrodynamic flow in a spiked electrode-plate electrostatic precipitator. *Journal of Electrostatics*, 69(5), 419-428. https://doi.org/10.1016/j.elstat.2011.06.002
- Fujishima, H., Ueda, Y., Tomimatsu, K., & Yamamoto, T. (2004). Electrohydrodynamics of spiked electrode electrostatic precipitators. *Journal of Electrostatics*, 62(4), 291-308. https://doi.org/10.1016/j.elstat.2004.05.006
- Ganesan, P., I., B., S., H., S., S., & Sandaran, S. C. (2016).

 Turbulent forced convection of Cu—water nanofluid in a heated tube: Improvement of the two-phase model. *Numerical Heat Transfer, Part A: Applications, 69*(4), 401-420. https://doi.org/10.1080/10407782.2015.1081019
- Goo, J. H., & Lee, J. W. (1997). Stochastic simulation of particle charging and collection characteristics for a wire-plate electrostatic precipitator of short length. *Journal of Aerosol Science*, 28(5), 875-893. https://doi.org/10.1016/S0021-8502(96)00475-2

- Hao, J., Kebin, H., & Chao, H. (1990). Calculation of electric field strength distributions for new electrostatic precipitator discharge electrode designs. *Journal of the Air & Waste Management Association*, 40(11), 1510-1513. https://doi.org/10.1080/10473289.1990.10466801
- He, X., Vázquez, P. A., & Zhang, M. (2023). Numerical analyses of wire-plate electrohydrodynamic flows. *Journal of Fluid Mechanics*, *966*, A4, Article A4. https://doi.org/10.1017/jfm.2023.419
- Iranshahi, K., Defraeye, T., Rossi, R. M., & Müller, U. C. (2024). Electrohydrodynamics and its applications: Recent advances and future perspectives. International Journal of Heat and Mass Transfer, 232, 125895. https://doi.org/10.1016/j.ijheatmasstransfer.2024.12
- Islamov, R. Sh. (2018). Influence of gas velocity on the particle collection and reentrainment in an aircleaning electrostatic precipitator. *Aerosol Science and Technology*, 52(12), 1415-1428. https://doi.org/10.1080/02786826.2018.1528003
- Jin, Y., Andersson, H., & Zhang, S. (2016). Air Pollution Control Policies in China: A Retrospective and Prospects. *International Journal of Environmental* Research and Public Health, 13(12), 1219. https://www.mdpi.com/1660-4601/13/12/1219
- Kallio, G. A., & Stock, D. E. (1992). Interaction of electrostatic and fluid dynamic fields in wire–plate electrostatic precipitators. *J. Fluid Mech*, 240., 133– 166. https://doi.org/10.1017/S0022112092000053
- Kihm, K. D. (1987). Effects of nonuniformities on particle transport in electrostatic precipitators. Standford University.
- Lee, E. M. (2024). Modeling of a novel large-scale electrohydrodynamic vortex flow induced by variation in current density for drag reduction with implication of electrostatic particle clustering. *Journal of Electrostatics*, 128, 103899. https://doi.org/10.1016/j.elstat.2024.103899
- Lei, H., Wang, L.-Z., & Wu, Z.-N. (2008). EHD turbulent flow and Monte-Carlo simulation for particle charging and tracing in a wire-plate electrostatic precipitator. *Journal of Electrostatics*, 66(3), 130-141. https://doi.org/10.1016/j.elstat.2007.11.001
- Leonard G. L., Mitchner M., & Self S. A. (1983). An experimental study of the electrohydrodynamic flow in electrostatic precipitators. *Journal of Applied Fluid Mechanics*, 127, 123–140. https://doi.org/10.1017/S0022112083002657
- Neimarlija, N., I., D., & Muzaferija, S. (2011). Numerical Method for Calculation of Two-Phase Electrohydrodynamic Flows in Electrostatic Precipitators. *Numerical Heat Transfer, Part A:* Applications, 59(5), 321-348. https://doi.org/10.1080/10407782.2011.549080

- Nikas, K. S. P., Varonos, A. A., & Bergeles, G. C. (2005). Numerical simulation of the flow and the collection mechanisms inside a laboratory scale electrostatic precipitator. *Journal of Electrostatics*, 63(5), 423-443. https://doi.org/10.1016/j.elstat.2004.12.005
- Oglesby, S. J., & Nichols, G. B. (1978). *Electrostatic precipitation*. Marcel Dekker Inc.
- Park, S. J., & Kim, S. S. (2000). Electrohydrodynamic Flow and Particle Transport Mechanism in Electrostatic Precipitators with Cavity Walls. *Aerosol Science and Technology*, 33(3), 205-221. https://doi.org/10.1080/027868200416204
- Parker, K. R. (2012). *Applied electrostatic precipitation*. Springer.
- Penney, G. W., & Matick, R. E. (1960). Potentials in D-C corona fields. *Transactions of the American Institute of Electrical Engineers, Part I: Communication and Electronics*, 79(2), 91-99. https://doi.org/10.1109/TCE.1960.6368550
- Podlinski, J., Berendt, A., & Mizeraczyk, J. (2013). Electrohydrodynamic secondary flow and particle collection efficiency in spike-plate multi-electrode electrostatic precipitator. *IEEE Transactions on Dielectrics and Electrical Insulation*, 20(5), 1481-1488. https://doi.org/10.1109/TDEI.2013.6633674
- Roache, P. J. (1994). Perspective: A Method for Uniform Reporting of Grid Refinement Studies. *Journal of Fluids Engineering*, 116(3), 405-413. https://doi.org/10.1115/1.2910291
- Friedlander, S. K. (2000). Smoke, Dust, and Haze: Fundamentals of Aerosol Dynamics. Oxford University Press.
- Sander, S., Gawor, S., & Fritsching, U. (2018). Separating polydisperse particles using electrostatic precipitators with wire and spiked-wire discharge electrode design. *Particuology*, 38, 10-17. https://doi.org/10.1016/j.partic.2017.05.014
- Schmid, H. -J., & Vogel, L. (2003). On the modelling of the particle dynamics in electro-hydrodynamic flow-fields: I. Comparison of Eulerian and Lagrangian modelling approach. *Powder Technology*, *135-136*, 118-135.
 - https://doi.org/10.1016/j.powtec.2003.08.009
- Shen, H., Yu, W., Jia, H., & Kang, Y. (2018). Electrohydrodynamic flows in electrostatic

- precipitator of five shaped collecting electrodes. Journal of Electrostatics, 95, 61-70. https://doi.org/10.1016/j.elstat.2018.08.002
- Shen, H., Jia, H., & Kang, Y. (2020). Electrical characteristics and electrohydrodynamic flows in electrostatic precipitator of six shaped discharge electrodes *Journal of Applied Fluid Mechanics*, 13(6), 1707-1718. https://doi.org/10.36884/jafm.13.06.31085
- Sivasankaran, S., & Mallawi, F. O. M. (2021). Numerical study on convective flow boiling of nanoliquid inside a pipe filling with aluminum metal foam by two-phase model. *Case Studies in Thermal Engineering*, 26, 101095. https://doi.org/10.1016/j.csite.2021.101095
- Skodras, G., Kaldis, S. P., Sofialidis, D., Faltsi, O., Grammelis, P., & Sakellaropoulos, G. P. (2006). Particulate removal via electrostatic precipitators CFD simulation. *Fuel Processing Technology*, 87(7), 623-631. https://doi.org/10.1016/j.fuproc.2006.01.012
- Soldati, A. (2000). On the effects of electrohydrodynamic flows and turbulence on aerosol transport and collection in wire-plate electrostatic precipitators. *Journal of Aerosol Science*, 31(3), 293-305. https://doi.org/10.1016/S0021-8502(99)00055-5
- Talaie, M. R. (2005). Mathematical modeling of wire-duct single-stage electrostatic precipitators. *Journal of Hazardous Materials*, 124(1), 44-52. https://doi.org/10.1016/j.jhazmat.2005.01.007
- Wang, G., Ma, Z., Deng, J., Li, Z., Duan, L., Zhang, Q., Hao, J., & Jiang, J. (2019). Characteristics of particulate matter from four coal-fired power plants with low-low temperature electrostatic precipitator in China. Science of The Total Environment, 662, 455-461. https://doi.org/10.1016/j.scitotenv.2019.01.080
- Yamamoto, T., Velkoff H. R. (1981).Electrohydrodynamics in electrostatic an precipitator. J. Fluid Mech, 108. 1–18. https://doi.org/10.1017/S002211208100195X
- Zhou, W., Jiang, R., Sun, Y., Chen, B., & Liu, B. (2021). Study on multi-physical field characteristics of electrostatic precipitator with different collecting electrodes. *Powder Technology*, *381*, 412-420. https://doi.org/10.1016/j.powtec.2020.12.028